Check for updates

The trials and triumphs of modelling X-ray absorption spectra of transition metal phthalocyanines†

Esma Birsen Boydas and Michael Roemelt ⓘ *

This study explores the electronic structure of Co, Fe and Mn phthalocyanines (TMPcs) as well as their perfluorinated counterparts through a series of electronic structure calculations utilizing multireference methods and by simulating their metal L-edge and ligand (nitrogen and fluorine) K-edge X-ray absorption spectra (XAS) in an angle-resolved manner. Simulations targeting different ground-state symmetries, where relevant, have been conducted to observe changes in the N K-edge lineshape. The applicability of the quasi-degenerate formulation of *n*-electron valence state perturbation theory (QD-NEVPT2) for L-edge X-ray absorption spectroscopy (XAS) is evaluated, alongside the use of a restricted active space (RAS) formalism to describe the final-state multiplets generated by L-shell X-ray processes. Our findings provide valuable insights into the electronic properties of TMPcs, in particular with respect to the effect of fluorination, and demonstrate the broad applicability of various formulations of NEVPT2 in spectral simulations. Moreover, this study highlights the utility of manual truncation of the configuration spaces in order to allow for large active orbital spaces in aforementioned calculations.

1 Introduction

Transition metal phthalocyanines (TMPcs) are a class of cyclic coordination compounds widely explored across multiple domains of chemistry due to their distinct structural, electronic, and magnetic properties.[1,2] These systems feature an 18-membered macrocycle composed of four isoindole units connected by carbon–carbon bonds. The first coordination shell of the central metal ion involves four nitrogen atoms, adopting a square planar configuration. Notably, TMPcs share structural similarities with porphyrins, essential components of biomolecules such as hemoglobin and chlorophyll.[3] Both porphyrins and phthalocyanines are able to accommodate over 70 elements at their central cavity while providing a rather rigid and stable coordination environment.[4]

TMPcs exhibit attractive electronic and magnetic characteristics owing to their extensive π-conjugation.[5] This skeleton facilitates electron delocalization throughout the entire macrocycle, resulting in pronounced absorption in the visible and near-infrared regions of the electromagnetic spectrum.[6] Such absorption properties render TMPcs appealing for diverse technological applications, including organic photovoltaics,[7] organic light-emitting diodes,[8] and sensors.[9] Besides their electronic attributes, TMPcs can also exhibit magnetic behavior due to their generally open-shell 3d orbital manifold.[10] This magnetic propensity positions TMPcs as pivotal constituents for novel materials and devices such as data storage and spintronics.[11,12]

Fluorinated metal–phthalocyanines (TMPcF16) are extensively employed across diverse applications.[13] In contrast to conventional p-type semiconductors such as TMPcs, TMPcF16 functions as an n-type semiconductor in photovoltaics and light-emitting diodes.[14] Furthermore, fluorination enhances the stability of these compounds, rendering them viable for operation in challenging environmental conditions.[15,16] The distinct electronic structure of TMPcF16 facilitates efficient charge transport, a fundamental aspect for optimal performance in electronic devices.[17]

The complex coordination chemistry of metallophthalocyanines offers compelling opportunities for the tunability of the electronic structure by altering the central metal ion or adding functional groups to the macrocycle. This adaptability allows for precise adjustments tailored to specific applications. A fundamental step in this direction involves elucidating the electronic structure of isolated TMPcs. This requires a comprehensive understanding of the arrangement of frontier molecular orbitals, spin states, ground state symmetry, and the nature

Institut für Chemie, Humboldt-Universität zu Berlin, Brook-Taylor-Str. 2, D-12489 Berlin, Germany. E-mail: michael.roemelt@hu-berlin.de; Tel: +49 (0)30 2093 82700

20376 | *Phys. Chem. Chem. Phys.,* 2024, **26**, 20376–20387

This journal is © the Owner Societies 2024

of near-degenerate states. For instance, in optimizing solar cell performance, it is crucial to thoroughly understand and adjust the energy levels of dye molecules.[18]

The electronic properties of first-row TMPcs have been extensively studied in the existing literature. Nickel and zinc phthalocyanines are commonly described as having a ground state electronic structure characterized by A_{1g} symmetry in a singlet spin state, as evidenced by several studies.[19–26] On the other hand, copper phthalocyanine is typically attributed to a $^2B_{1g}$ state.[27–31] The consensus among these studies provides strong support for the ground state electronic structures of NiPc, ZnPc, and CuPc.

In contrast, a considerable disparity exists when it comes to the identity of the ground and low-lying excited states of the corresponding cobalt, iron, or manganese complexes. This discrepancy is evident across several studies.[32–35] Specifically regarding MnPc, experimental observations suggest that differences in sample preparation can result in different spatial symmetries being assigned to the ground state, primarily varying between $^4A_{2g}$ and ^4E_g states.[35] The discrepancies concerning CoPc and FePc primarily revolve around the thermally accessible near-degenerate states.[35–37]

Considering the susceptibility of these complexes to various near-degenerate states, and the inconsistency often observed in DFT-based studies due to the choice of density functional, it is valuable to highlight previous studies that employed multi-configurational wavefunction based methods. For example, Wallace *et al.* recently conducted a study scrutinizing the ground state electronic structure of TMPcs to assign state symmetries at a CASSCF and MRMP2 level.[38] The active spaces in this study included metal 3d orbitals along with a small number of significant ligand orbitals. Structure optimizations were performed at the B3LYP/6-31G* level only for ZnPc, with its geometry then used as a model scaffold for the remaining TMPcs. This decision was based on previous X-ray diffraction data indicating no discernible differences in the first-coordination shell of TMPcs across the sequence from MnPc to ZnPc. In a subsequent study by Hobza *et al.*, much larger active spaces, such as CASPT2/CASSCF (16e,15o) and DMRG(28e,36o), were employed to shed light on the spin-state of iron phthalocyanine.[39] Here, a quintet ground state was found to be thermally stable for an isolated FePc moiety in the gas phase.

Building upon the extensive literature on TMPcs, this work aims to unravel the characteristics of the ground and low-lying excited states of multiple TMPcs utilizing transition metal L-edge and ligand K-edge X-ray absorption spectra as means of validation of the obtained results. The first part of this study concerns the local electronic structure of 5 TMPcs shown in Fig. 1, *i.e.* dominating electronic configurations are reported for all low-energy states as obtained from state-of-the-art multireference electronic structure methods. Then, computed nitrogen K-edge spectra are compared to the experimentally observed spectra. In this way, the results from the first part are validated and the observed features in the spectra can be assigned to electronic transitions. In a similar manner, the less
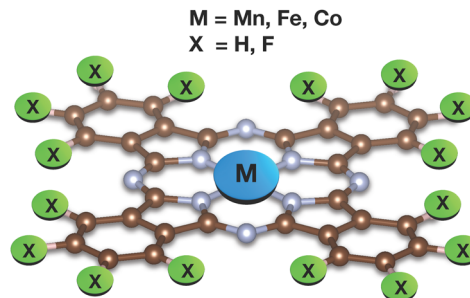

M = Mn, Fe, Co
X = H, F

Fig. 1 Illustration of the cobalt dioxolene compounds studied in this work.

well studied F K-edges of CoPcF16 and FePcF16 have been computed and analyzed. Finally, after having established confidence in the symmetry and spin state of the electronic ground state description, the complex task of modeling L-edge multiplets is effectively pursued. Here, the transition metal L-edge spectra have been modelled by means of Complete Active Space Configuration Interaction combined with strongly contracted *n*-electron valence perturbation theory (SC-NEVPT2) and its quasi-degenerate (QD-NEVPT2) variant.[40–42] To accommodate larger active spaces while simulating the L-edges, a manual truncation of the final state multiplets has also been carried out. In some cases, the comparison between calculated and experimentally observed spectra indicates interesting features of the experimental setup, *e.g.* the presence or absence of significant chemical interactions between the investigated TMPc and the surface it has been adsorbed on.

2 Computational methodology

A series of simulations were conducted employing various theoretical levels, primarily utilizing the ORCA software package version 4.2.[43] The subsequent paragraphs will describe these setups.

2.1 Structure optimizations

Geometry optimizations were executed using the B3LYP global hybrid density functional[44,45] alongside the def2-TZVP(-f) basis set,[46] with numerical integration facilitated by a dense grid (ORCA Grid5). Acceleration of Coulomb and exchange integrals was achieved through the resolution of identity (RI) and chain-of-sphere (COSX) approximations, in conjunction with the def2/J basis set.[47–52] Additionally, dispersion corrections were incorporated using the D3BJ method.[53,54]

2.2 Ligand K-edge

Nitrogen and fluorine K-edge XAS were simulated using time-dependent density functional theory (TD-DFT) calculations, permitting the excitation of electrons from molecular orbitals with a primary ligand 1s character.[55] The N 1s orbitals were localized using the Pipek–Mezey scheme to simulate the underlying phenomena.[56] The Tamm–Dancoff approximation (TDA) was employed in all TD-DFT calculations,[57] and scalar

This journal is © the Owner Societies 2024

Phys. Chem. Chem. Phys., 2024, **26**, 20376–20387 | **20377**

relativistic effects were approximated using the zeroth-order regular approximation (ZORA).[58–60] Simulated spectra were generated by convoluting the calculated transitions with Gaussian functions of 0.3 to 1.0 eV width. All computed spectra were shifted by around 12 eV to better align with experimental counterparts, a necessary adjustment to account for systematic errors introduced by the TD-DFT method and dependent on the chosen functional and basis set.[55]

2.3 Transition metal L-edge

2.3.1 CASCI/NEVPT2. Transition metal L-edge spectra were computed using two distinct levels of theory: CASCI/NEVPT2 and RASCI. The CASCI/NEVPT2 approach involved optimizing a valence active space of metal 3d-based orbitals in a state-averaged CASSCF fashion, followed by a CASCI calculation with energy refinement incorporating dynamic electron correlation effects *via* strongly contracted or quasi-degenerate second-order *n*-electron valence perturbation theory (SC-NEVPT2 or QD-NEVPT2).[40,41] This multi-step protocol for L-edge spectroscopy underwent thorough validation for first-row transition metal atoms in prior research by Chantzis *et al.*[61] Additionally, spin–orbit coupling effects were addressed using quasidegenerate perturbation theory (QDPT), with the spin–orbit mean-field approximation applied during the evaluation of SOC matrix elements.[62] Scalar relativistic effects were accounted for in all steps of the L-edge spectra calculations *via* the second-order Douglas–Kroll Hess (DKH2) correction, while utilizing finite nucleus model.[63–65] The cc-pVTZ-DK basis set was chosen to be consistent with the benchmark study by Chantzis *et al.*,[61,66–68] and two-electron integrals were computed using the resolution of the identity (RI) approximation with an automatically generated auxiliary basis set.[69] All computations were performed in the gas phase while excluding considerations of potential interactions with neighboring molecules.

2.3.2 RASCI with ligand orbitals. The systems under investigation in this study feature a complex valence orbital structure due to numerous π orbitals from ligands. Selecting an appropriate active space and managing core-excited state multiplets poses a considerable challenge for these kind of systems. Calculating a wealth of final-state multiplets while considering dynamic electron correlation within a large acceptor orbital space, capable of capturing essential electronic structure, requires significant computational resources. Therefore, we utilized the RASCI method along with the recently developed ASS1ST strategy.[70,71] This approach aimed to identify active spaces that include all strongly correlated orbitals while remaining as compact as possible.

The ASS1ST method generates a set of quasi-restricted natural orbitals for both internal and external orbital spaces. The correlation strength of these natural orbitals is determined by their associated natural orbital occupation numbers (NOONs), providing insights into whether to include or exclude them from the active space. Initially, the active space consisted solely of metal 3d orbitals.

In RASCI part, the orbital optimization of valence excited states included the ligand-based a_{1g} orbital, the doubly
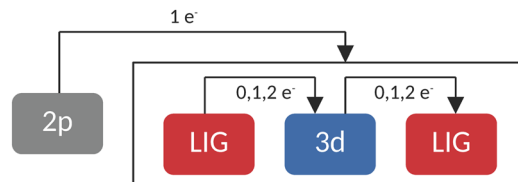

Fig. 2 Schematic representation of the configuration space used in restricted active space calculations.

degenerate LUMOs of e_g character, and the transition metal 3d orbitals in the active space. On these optimized orbitals, a configuration interaction (CI) calculation with manually selected configurations (CFGs) has been carried out. A schematic representation of the employed configurations can be seen in Fig. 2. This setup accounted for up to double excitations from (and to) the ligands in the final state multiplets. While resembling previous works by Lundberg *et al.*, where a SA-RASSCF orbital optimization was followed by a RASPT2 treatment with appropriate ionization potential electron affinity (IPEA) shifts and imaginary shifts, our study employed a SA-CASSCF orbital optimization and a manually truncated selected configuration interaction step.

2.4 Comparison of simulated and experimental spectra

When comparing simulated and experimental X-ray spectra, one can employ various methods. These approaches usually involve examining the numbers, positions, and approximate heights or areas of calculated spectral features and comparing them with their counterparts in experimental spectra in a qualitative manner. Additionally, more quantitative techniques, such as direct least-squares comparison or similarity scores are commonly used. However, it's important to recognize that achieving perfect alignment between calculated and experimental spectra may be challenging due to difficulties in accurately modeling macroscopic effects such as hybridizations at the interface or bulk effects. Therefore, we opt not to use similarity or distance scores in our comparisons.

The macroscopic effects mentioned earlier can appear in various ways in X-ray spectroscopy, especially when studying adsorbates on surfaces. To illustrate potential scenarios, consider the case of transition metal phthalocyanines (TMPcs) grafted onto a surface, as shown in Fig. 3. The primary focus of this work is on modeling an isolated phthalocyanine moiety (case A). However, in experimental setups, TMPcs are often attached to metallic or nonmetallic surfaces as thin films, which can vary in thickness. For instance, a monolayer (case
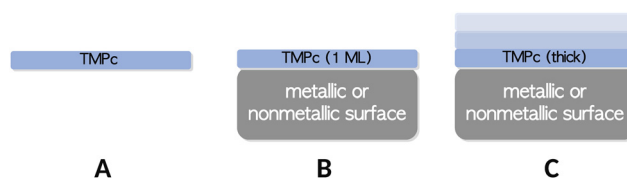

Fig. 3 Schematic representation of isolated TMPcs and as adsorbates on metallic or nonmetallic surfaces.

20378 | *Phys. Chem. Chem. Phys.*, 2024, **26**, 20376–20387

This journal is © the Owner Societies 2024

B) may highlight surface–TMPc interaction effects, while thicker films (case C) predominantly reflect interactions among the TMPc layers themselves. It is crucial to recognize that achieving a one-to-one mapping between simulated and experimental spectra cannot ba achieved, especially when dealing with a reactive surface, such as Ag(111).[72]

3 Results and discussion

The scrutinized systems maintain a planar structure with a D_{4h} point group symmetry. Yet, symmetry was neither enforced nor utilized during any of the reported calculations. The metal ions are coordinated by four nitrogen atoms originating from pyrrole units. Additionally, these four pyrrole entities are linked to a tetradentate ligand *via* four additional nitrogen atoms located in meso positions. Consequently, two distinct groups of nitrogen atoms are discernible, denoted as N_{pyr} and N_{aza} (see Fig. 4). The nomenclature for these non-equivalent nitrogens is derived from a prior theoretical investigation on metal phthalocyanines (Pcs) by De Francesco *et al.*[73] Additionally, for the fluorine K-edge calculations of fluorinated metallophthalocyanines, it is pertinent to distinguish between two different types of fluorine atoms: F_{inner} and F_{outer}.

3.1 Ground state electronic structure

Equilibrium structures. A summary of the important bond lengths belonging to the first- and second-coordination shells of the optimized metallophthalocyanines is given in Table 1. These results align closely with both the experimental crystal structures and previous theoretical works.[74,75] The bond distances of N_{aza}–C were not affected by the presence of different
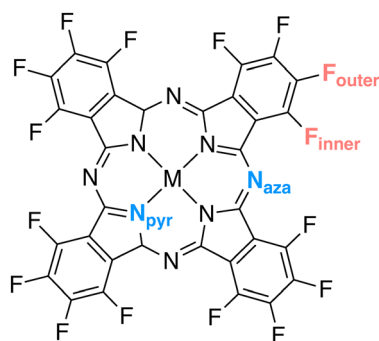

Fig. 4 Schematic representation of N_{pyr}, N_{aza} in all tested molecules, and F_{inner} and F_{outer} in fluorinated metallophthalocyanines.

Table 1 The important bond lengths (Å) of first- and second-coordination shells of TMPcs. (B3LYP/def2-TZVP(-f) level of theory has been utilized in structure optimizations)

Name	M–N	N_{pyr}–C	N_{aza}–C
CoPc	1.93	1.38	1.32
FePc	1.94	1.37	1.32
MnPc	1.95	1.38	1.32
CoPcF16	1.93	1.38	1.32
FePcF16	1.94	1.39	1.32

Table 2 Ground state electronic structure of TMPc's in terms of their possible state symmetries and 3d orbital occupancies. (CASSCF/NEVPT2 involving Gouterman-like orbitals and metal 3d manifold)

Metal ion	State symmetry	Main configuration
Mn	$^4A_{2g}$	$(d_{xy})^2(d_{xz}, d_{yz})^{1,1}(d_{z^2})^1$
	^4E_g	$(d_{xy})^1(d_{xz}, d_{yz})^{2,1}(d_{z^2})^1$
	$^4B_{1g}$	$(d_{xy})^1(d_{xz}, d_{yz})^{1,1}(d_{z^2})^2$
Fe	$^3A_{1g}$	$(d_{xy})^2(d_{xz}, d_{yz})^{1,1}(d_{z^2})^2$
	^3E_g	$(d_{xy})^2(d_{xz}, d_{yz})^{2,1}(d_{z^2})^1$
	$^3B_{2g}$	$(d_{xy})^1(d_{xz}, d_{yz})^{2,2}(d_{z^2})^1$
Co	$^2A_{1g}$	$(d_{xy})^2(d_{xz}, d_{yz})^{2,2} (d_{z^2})^1$
	^2E_g	$(d_{xy})^2(d_{xz}, d_{yz})^{2,1}(d_{z^2})^2$

transition metal ions, and found to be 1.32 Å for all molecules tested. The metal–N and N_{pyr} distances across different TMPcs were within 0.01 Å.

State symmetry. A brief overview of the ground state electronic structure of MnPc, FePc, and CoPc is provided in Table 2. This table includes state symmetry labels and the dominating electronic configurations for ground and low-lying excited states. These states are found to be within 1 eV of their corresponding CASSCF ground states. It is worth noting that different theoretical methods may yield varying energy orderings, as reported in existing literature.[38] However, our results from CASSCF, along with previous findings using MR-MP2,[38] indicate consistent state compositions.

The ASS1ST scheme has been employed across all complexes to investigate the ground state correlation and observe changes in the electronic structure of TMPcs when different transition metals are incorporated. As described elsewhere in detail,[70,71] ASS1ST predicts how strong orbitals are correlated by computing approximate natural orbital occupation numbers. The farther apart this number is from 2 or 0, the more correlated the corresponding orbital is. This approach also aids in selecting a suitable active space for these compounds. The starting point for all reported ASS1ST calculations was a minimal CAS comprising only metal 3d orbitals.

The results for CoPc are presented in Fig. 5. Metal 3d orbitals of $(d_{xy})^2(d_{xz}, d_{yz})^{2,2}$ display an occupation of 2.0. In the case of CoPc, this configuration corresponds to the $^2A_{1g}$ state. Additionally, Gouterman-like orbitals from both internal (1.93, 1.96) and virtual subspaces (doubly-degenerate 0.05) are easily discernible. These results indicate that the desired $^2A_{1g}$ state has been successfully located through ASS1ST calculations.

The ASS1ST plots for FePc and MnPc are available in the ESI.† One of the most debated phthalocyanines, FePc, was found to be of ^3E_g state, in line with the previous theoretical studies that utilized B3LYP, and experimental studies employing FePc thin films.[76,77] For MnPc, the ASS1ST simulations predominantly point to the $^4A_{2g}$ state with a $(d_{xy})^2(d_{xz}, d_{yz})^{1,1}(d_{z^2})^1$ configuration. Notably, orbitals with occupation numbers around 0.05 and 0.055 indicate a loss of degeneracy in the Gouterman-like orbitals from the virtual space due to Jahn–Teller (JT) distortion. This suggests involvement from the
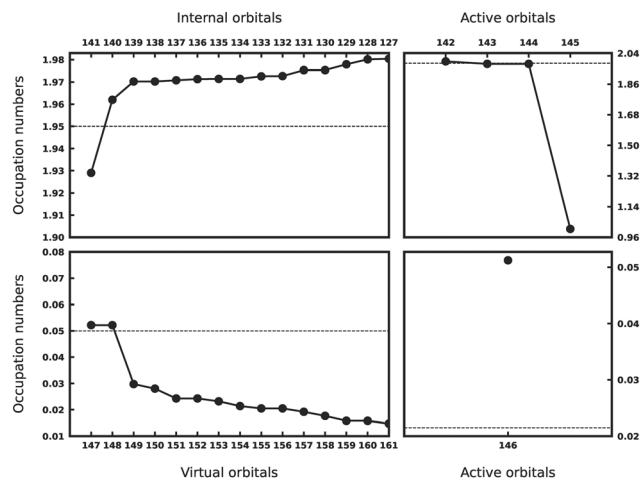
This journal is © the Owner Societies 2024

Phys. Chem. Chem. Phys., 2024, **26**, 20376–20387 | **20379**

Fig. 5 ASS1ST scheme for CoPc.

^4E_g state. A JT effect is not observed for the other molecules. Furthermore, there is an evident increase in the active orbital character when transitioning from Co to Mn, while the remaining orbitals from the internal subspaces maintain a similar character across this sequence.

ASS1ST results for the fluorinated phthalocyanines CoPcF16 and FePcF16 can be found in the ESI,† Fig. S1 and S4. Both CoPcF16 and FePcF16 exhibit a behavior similar to their non-fluorinated counterparts, CoPc and FePc, respectively, with one notable difference: the occupation numbers of the Gouterman-like virtual orbitals (also referred to as π-backbonding type ligands) are smaller in the fluorinated compounds. This difference can be attributed to the electron-withdrawing effect of fluorine substitution, which stabilizes the HOMO and destabilizes the LUMO.[78] As a result, there is a weaker correlation of these orbitals in the ground state of the fluorinated compounds.

3.2 Ligand K-edges

3.2.1 Nitrogen K-edge. In prior investigations, the nitrogen K-edges of CuPc, CoPc, and FePc have been modeled using various levels of theory, including time-dependent density functional theory (TDDFT) with Slater type orbitals (STOs), TDDFT with Gaussian type orbitals (GTOs), and transition state Kohn–Sham density functional theory (TS-KS DFT) in different studies.[31,73,79–81] In this section, we examine the spectral region for CoPc, FePc, and MnPc also using TDDFT, with particular attention to the influence of different central metal ions and underlying transitions in the spectra, analyzed in an angle-resolved manner. Fig. 6 presents a comparison between experimental and calculated spectra for the nonfluorinated TMPcs. The analysis distinguishes between two distinct groups of nitrogen atoms within the system, designated as N_{aza} and N_{pyr}. A total of 500 roots originating from eight different nitrogen 1s orbitals has been calculated for the isolated TMPc molecules.

3.2.1.1 Lineshape and origins. Nitrogen K-edge of CoPc, FePc and MnPc display three evident peaks in their π* region, as indicated in Fig. 6 by labels A, B, and C. CoPc and FePc exhibit similar lineshapes, while the experimental spectrum of MnPc is somewhat different. Noteworthy differences of MnPc include more pronounced shoulder features at peaks A and B, with peak B displaying a notable redshift in comparison to CoPc and FePc. Peak A originates from intense 1s-to-π* Gouterman orbital transitions, arising from either N_{aza} or N_{pyr}. This phenomenon can be attributed to the stabilization of π-backbonding-type e_g orbitals in MnPc, which is also evident in the ground-state molecular orbital (MO) representation, as illustrated in Fig. 2 of ref. 38. The corresponding NDOs of the nitrogen K-edge simulations are detailed in ESI.†

3.2.1.2 CoPc. As mentioned previously, conflicting reports about the identity of the electronic ground state of CoPc can be found in the literature with the most prominent candidates being $^2A_{1g}$, ^2E_g or a mixture of both.[82] Fig. 6 presents the Co K-edge simulation for the $^2A_{1g}$ state, while the corresponding simulation for ^2E_g state can be found in the ESI,† Fig. S6. Our results indicate the presence of a $^2A_{1g}$ ground state, as this provides better agreement with the experimental nitrogen K-edge. The lineshape at the grazing angle for the ^2E_g state shows a minor shift of peak B to lower energies. Additionally,
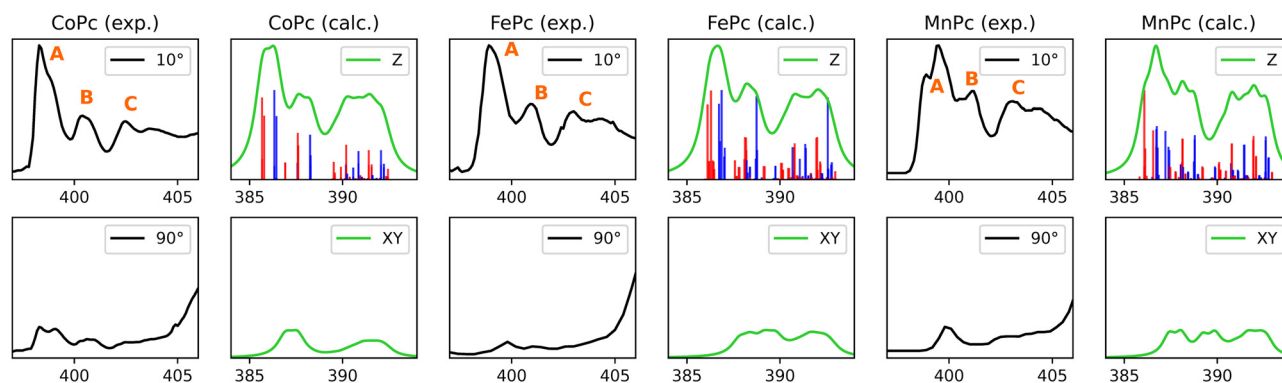

Fig. 6 Experimental (black) and calculated (green) nitrogen K-edge XAS for TMPcs. Energies are given in electronvolts, and the intensities are normalized. (The $^2A_{1g}$ state of CoPc could only be located when a restricted open-shell Kohn–Sham (ROKS) wavefunction is employed, and these orbitals were fed into the TDDFT calculations without further iterations.)

20380 | *Phys. Chem. Chem. Phys.*, 2024, **26**, 20376–20387

This journal is © the Owner Societies 2024

the in-plane transitions are shifted to a higher energy regime due to the unavailability of the d_{z^2} orbital.

3.2.1.3 FePc. The calculated N K-edge in Fig. 6, refers to a FePc of ^3E_g symmetry, whereas the simulations from the $^3A_{1g}$ state are given in ESI,† Fig. S7. In this case, all experimentally observed features within the π*-range, along with the relative intensity of transitions, are successfully reproduced for both ground state symmetries.

3.2.1.4 MnPc. A remarkable agreement between calculations and the experiment is observed for MnPc. This is somewhat surprising as the presented calculations only take into account an isolated MnPc molecule and intermolecular interactions have been reported to considerably affect the electronic structure of MnPcs.[83–85] The ground state symmetry employed herein is ^4E_g with $(d_{xy})^1(d_{xz}, d_{yz})^{2,1}(d_{z^2})^1$ configuration, which is also in line with previous XAS, MCD and UV-Vis measurements.[33,86–88]

3.2.2 Fluorine K-edge of CoPcF16. Compared to nitrogen K-edge studies, fluorine K-shell investigations are less common. Previous studies have explored derivatives of formaldehyde[89] and utilized both non-resonant and resonant X-ray setups on sulfur hexafluoride.[90,91] In the domain of porphyrins, Mangione *et al.* conducted two consecutive studies investigating the fluorine K-edge of CuTPP and CuTPP(F), while employing TDDFT simulations to elucidate the experimental spectra.[92,93] Interpreting experimental F K-edges poses a challenge due to the co-occurrence of 1s-π* and 1s-σ* transitions within the same energy range.[94,95] This complexity can complicate the analysis of planar compounds, despite their structural anisotropy often being advantageous in many X-ray regions.[96] In such cases, simulations play a crucial role in understanding the spectra and assigning observed bands to electronic transitions. This subsection provides a detailed analysis of the F K-edge of CoPcF16 and FePcF16. Similar to the nitrogen K-edges, a nomenclature has been used to distinguish between different fluorine moieties. A schematic representation of F_{inner} and F_{outer} is shown in Fig. 4. It should be noted, that our categorization does not account for Jahn–Teller (JT) distortion and the concomitant destruction of site symmetry. After JT distortion, all four fluorine atoms are, in principle, inequivalent. However, considering the 16 fluorine 1s orbitals separately in calculations becomes impractical. Therefore, a JT-description is omitted, and only two inequivalent fluorine 1s orbitals were used in the donor space, with 500 excited state roots from these orbitals taken into account in the TDDFT calculation.

The experimental F K-edge spectra of CoPcF16 and FePcF16 presented in Fig. 7 (CoPcF16) and ESI,† Fig. S9 (FePcF16) were obtained from previous studies conducted on Au(100) and Cu(111) surfaces, respectively.[94,97] They show similar relative intensities for both the σ* and π* ranges. Additionally, a noticeable difference between the F K-edge spectra at 0.5 nm and 3.0 nm thicknesses is observed in the experiment, whereas the calculated spectra closely resemble that of the 3.0 nm thickness. This observation suggests significant hybridizations occurring at the interface. Despite the similarity in lineshape,
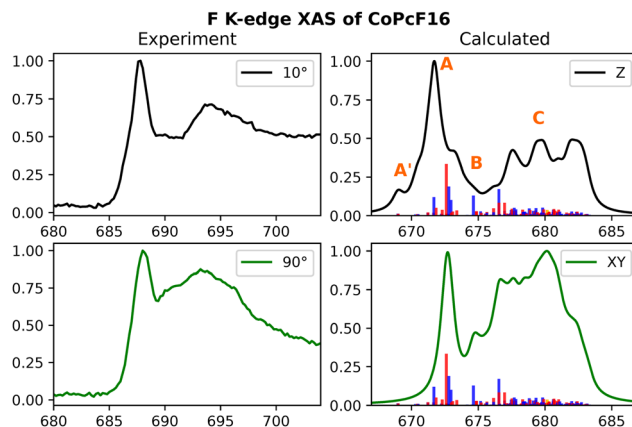

Fig. 7 Experimental and calculated F K-edge spectra for CoPcF16. Only one 1s orbital per fluorine–type (F_{inner} and F_{outer}) has been taking into account. The experimental results were adapted from a previous study on Au(100) surfaces.[97]

it is evident from the spectra at 10 degrees and the calculated spectrum that the C–F bonds are not entirely parallel to the surface.[94]

Referring to the origins of individual features, the low-energy small shoulder is denoted as A′, the mainline as A, the less-intense feature around 690 (675) in the experiment (calculated) as B, and the higher energy broad band as C. The low-energy shoulder A′ primarily consists of the ligand-centered e_g-type acceptor orbitals mixing with the transition metal $3d_{xz}$ and $3d_{yz}$ orbitals in an anti-bonding fashion. For FePcF16, these transitions are found to be slightly more intense in the calculations. A closer look into the energetic positions of the aforementioned transitions can be found in ESI,† Fig. S10. The main feature at around 688 eV in the experiment stems from both π* and σ* based transitions. The NDO isodensity plots for the intense transitions are provided in ESI,† Fig. S16 (CoPcF16) and Fig. S17 (FePcF16).

3.3 Transition metal L-edges

Various approaches have been employed in prior research to simulate the L-edge region of metallophthalocyanines. For instance, Zhou and colleagues utilized ligand field multiplet calculations to focus on crystal field parameters for CoPc, determining its ground state symmetry to be 73% $^2A_{1g}$ $3d^7$ character and 27% $3d^8\underline{L}$ component.[75] Another study by Zhang *et al.* explored the structural anisotropy of CoPc films on Au(111) surfaces, employing multiplet ligand-field theory to analyze in-plane and out-of-plane transitions.[82] Similar approaches have been applied to FePc simulations, where a ^3E spin ground state is predominant.[79,98] Recently, Lüder introduced a machine learning concept utilizing an artificial neural network (ANN) trained on a vast spectral database,[99] while Carlotto *et al.* employed a DFT/ROCIS approach, suggesting ground state symmetries for MnPc and FePc based on DFT energetics from the BP86 functional.[86]

In the present study, L-edge XAS was simulated using complete and restricted active space methods to accommodate

This journal is © the Owner Societies 2024

Phys. Chem. Chem. Phys., 2024, **26**, 20376–20387 | **20381**

Table 3 Included number of roots for each multiplicity block in the final L-edge spectra by means of CASCI/NEVPT2 calculations

TMPc	Active space	Multiplicity	Nroots	SOCroots
CoPc	(13,8)	4, 2	40, 115	390
FePc	(12,8)	5, 3, 1	35, 195, 170	930
MnPc	(11,8)	6, 4, 2	16, 174, 360	1512

the multiplets generated by 2p to 3d excitations. The valence active space consisted of metal-based 3d orbitals in a CASCI/NEVPT2 setup. In RAS calculations of FePc and MnPc, the active space was extended to include ligand-based HOMO, HOMO−1, and doubly degenerate LUMO orbitals.

3.3.1 CASCI/NEVPT2. The CASCI/NEVPT2 setup entails the computation of numerous excited state roots. Table 3 provides details on the number of nonrelativistic states, their respective multiplicities, and the total count of spin–orbit coupled roots.

3.3.1.1 CoPc. A comparison between experimental and calculated Co L-edge XAS spectra for CoPc is presented in Fig. 8. In addition to the strongly contracted variant of NEVPT2, the quasidegenerate formulation has also been examined, depicted in blue. The normalized total spectrum from calculations is compared with experimental data taken at an angle of 50 degrees. Features labeled (A–E) observed in the experiment at 90 degrees are marked in the subplot. The low-energy peak A at approximately 779 eV in the experiment intensifies as the beam angle transitions from 90 to 10 degrees, indicating contributions from both in-plane and out-of-plane components. Conversely, the intensity of peaks B and C decreases at grazing incidence angles. While the CASCI-based calculated spectrum provides a reasonable representation, the lineshapes suggest the need for energy refinement through dynamic electron correlation methods. Upon applying the strongly contracted version of NEVPT2, additional features emerge. Notably, all features observed in the experimental data are replicated in the spectra calculated using QD-NEVPT2. There exists a minor discrepancy in the intensity ratio of peaks B and C. However, considering that the experimental spectra involve a 3 nm thick film of CoPc while the calculation refers to an isolated

CoPc molecule in the gas-phase, the agreement is astonishingly good.

The ground state identified at the CASCI level manifests as a spin quartet. However, following the NEVPT2 treatment, the $^2A_{1g}$ state emerges as the lowest energy state, underscoring the significance of dynamic electron correlation. In examining the excited states and their compositions contributing to peaks A–E, particular attention is given to the outcomes obtained with QD-NEVPT2, given its noteworthy alignment with experimental spectra. Notably, a single spin–orbit-coupled (SOC) transition in the low-energy range gives rise to peak A, comprising 80% $2p_{x,y}$ to $d_{x^2-y^2}$ and 13% $2p_z$ to d_{z^2} excitations. The predominant in-plane character of this transition results in a high-intensity feature at grazing angles, while a weaker out-of-plane component is still discernible at 90 degrees. Features B–C–D encompass multiple out-of-plane transitions involving the d_{z^2} orbital, exhibiting a notable decrease in intensity at grazing angles. Interestingly, feature E at higher energies is also successfully reproduced using a relatively minimal active space comprising solely 2p and 3d orbitals. These transitions are ascribed to SOC-coupled doublet + quartet type excitations characterized by various multiplet attributes.

3.3.1.2 FePc. The experimental and calculated Fe L-edge XAS spectra are depicted in Fig. 9. A Pc film thickness of 3 nm has been selected to rule out the interface hybridization effects (*vide supra*).[72] Notably, features A–E are highlighted in the experimental spectra acquired at a 90-degree angle. Upon transitioning from a 90-degree to a 10-degree beam angle, feature A diminishes in intensity, while peak B assumes prominence as the mainline. Towards the higher energy range, features C–D–E exhibit reduced intensity at grazing angles.

Interestingly, a notable discrepancy between the experimental data and QD-NEVPT2 calculations is evident. Specifically, the calculated spectra at 50 and 10 degrees diverge significantly from their experimental counterparts. In contrast, the CASCI spectrum at 10 degrees bears a striking resemblance to the experimental data. This observation may suggest that while the valence active space captures crucial orbitals contributing to out-of-plane transitions, it may lack a
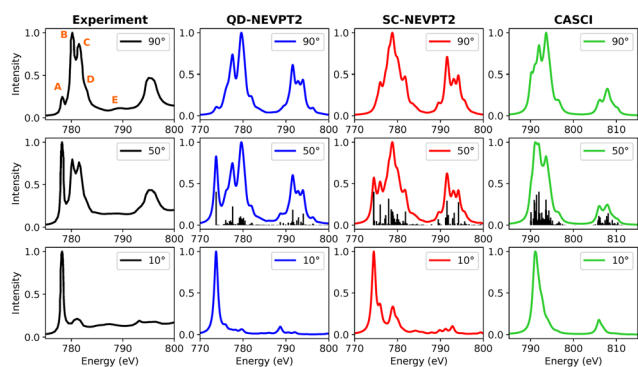

Fig. 8 Experimental and calculated Co L-edge XAS for CoPc. The experimental results were adapted from a previous study on Ni(111) surfaces.[100]
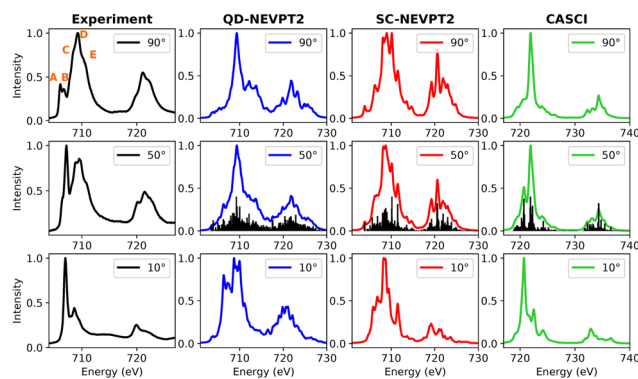

Fig. 9 Experimental and calculated Fe L-edge XAS for FePc. Only the L_3 edge is shown. The experimental results were adapted from a previous study by Peisert *et al.*[72]
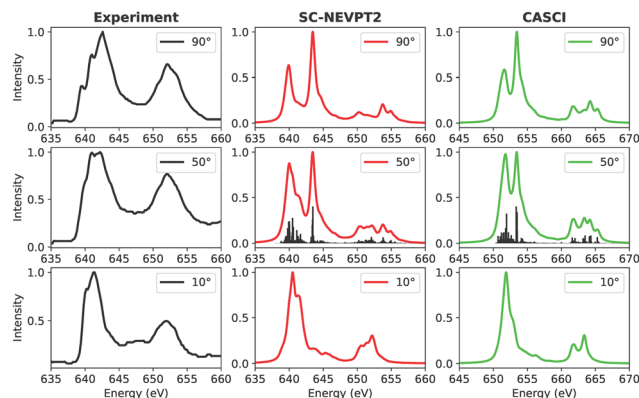
20382 | *Phys. Chem. Chem. Phys.,* 2024, **26**, 20376–20387

This journal is © the Owner Societies 2024

Fig. 10 Experimental and calculated Mn L-edge XAS for MnPc. The experimental results were adapted from a previous study on Ag(111) surfaces.[101]

Fig. 11 Experimental and calculated Fe L-edge XAS for FePc. The experimental results were adapted from a previous study by Peisert et al.[72]

comprehensive description of spectroscopically relevant in-plane orbitals.

The disparity observed between the experimental results and simulations may stem from various contributing factors. An irregular deposition of FePc moieties on the surface or significant hybridization between FePc layers could influence the observed spectra. Additionally, from a theoretical perspective, the size of the selected valence active space, crucial for characterizing the acceptor orbital manifold, is often a subject of debate. Consequently, to address these potential issues, a RASCI description incorporating additional ligand orbitals has been explored in Section 3.3.2.

3.3.1.3 MnPc. Manganese phthalocyanine (MnPc) stands out for having the highest number of available (unoccupied) 3d states among the considered set of TMPcs, leading to a multitude of final states upon excitation. Accordingly, the number of calculated roots is significantly higher than in the other cases (see Table 3) thereby prohibiting the application of the QD-NEVPT2 Ansatz owing to its high computational cost that scales quadratically with increasing number of roots.

In the experimental spectrum of MnPc, a broad L_3 peak is evident at a beam angle of 90 degrees, as depicted in Fig. 10. The experimental data correspond to a 3.2 nm thick Pc layer and reveal three main features in the L_3-edge, which reduce to two at grazing incidence. A similar trend is discernible in the spectra based on SC-NEVPT2, where features A and B intensify with a shift in the incidence of the synchrotron light from 90 to 10 degrees, albeit with slightly misaligned intensity ratios. Similar to the FePc case, the CASCI-based spectrum at 10 degrees provides a satisfactory representation at the grazing angle, yet the agreement is inadequate at 90 degrees of incidence. It is crucial to note the considerable variation in the L-edge spectra of MnPc, dependent on factors such as the thickness of the Pc layer and the surface used, thereby complicating the analysis. Hence, it is reiterated that a direct one-to-one mapping between the experiment and simulations may be impossible without taking into account the underlying surface.
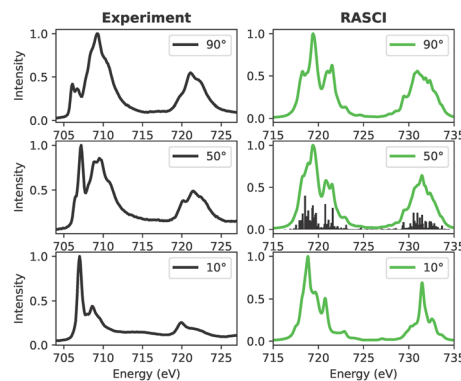
3.3.1.4 The effect of fluorination. In a study by Balle et al.,[102] the L-edge XAS of fluorinated CoPc on Cu-intercalated surfaces was investigated. The thin film of CoPcF16, with a thickness of 3 nm, displayed spectral features similar to those of CoPc. A similar observation was made for FePcF16 on rutile TiO_2 surfaces.[103] Fig. S18, ESI† depicts the calculated L-edge XAS of CoPcF16, with the spectra for CoPc shown in grey for comparison. Despite minor variations in the relative intensities of the features, the calculated spectra did not reveal any additional peaks.

3.3.2 RASCI. The RASCI-based L-edge spectrum of FePc is depicted in Fig. 11, alongside the experimental spectra. As outlined above, the RASCI calculations utilize a larger active space involving ligand based orbitals but neglect dynamic electron correlation. Notably, compared to the CASCI spectrum shown in Fig. 9, the agreement between experiment and calculation increases significantly thus underlining the importance of ligand based orbitals for the Fe L-edge. Notably, the structure of the calculated spectra around 709 eV at 50 and 90 degrees improved. For MnPc the influence of ligand-based orbitals on the L-edge spectrum depends on the angle as is illustrated in ESI,† Fig. S21. Inclusion of ligand-based orbitals *via* the RASCI approach leads to visibly improved albeit not perfect agreement between experiment and calculation at 90 and 50 degree. In contrast, at 10 degree SC-NEVPT2 seems to reproduce the experimental spectrum better. Additional research that goes beyond the scope of this work is necessary to explore the possibilities and limitations of the RASCI Ansatz for reproducing transition metal L-edges.

4 Conclusions

This work provides an in-depth theoretical study of the electronic structure of a series of transition metal phtalocyanines with a particular emphasis on their ligand K-edge and transition metal L-edge absorption spectra. The different spectra for cobalt, iron, and manganese phthalocyanines have been simulated using tailored theoretical approaches, each designed for their respective spectral regions. Remarkable agreement between the TDDFT-calculated ligand K-shell spectra and

This journal is © the Owner Societies 2024

Phys. Chem. Chem. Phys., 2024, **26**, 20376–20387 | **20383**

experimental data is observed, particularly regarding their structural anisotropy. Different ground-state symmetries have been taken into account in the simulations where needed, and $^2A_{1g}$, ^3E_g and ^4E_g states for Co, Fe and Mn centered phthalocyanines were found to be in agreement with the K-edge XAS of >2 nm thick films of TMPcs on various surfaces. The simulation of the fluorine K-edge of CoPcF16 and FePcF16, conducted for the first time, also showed success in reproducing the experiment, despite using only isolated metallophthalocyanines. While this spectral region for the TMPcF16 scaffold involves numerous transitions of both σ^* and π^* character within similar energy ranges, no noticeable difference in anisotropic characteristics across different transition metals was observed, except for the intensity ratio of the low-energy feature. This low-intensity shoulder present in the calculations shifted towards lower energy levels and exhibited increased intensity, particularly in the case of FePcF16. This difference constitutes the sole disparity noted within the experimental lineshape for the fluorine K-edge XAS.

Modeling the L-edge XAS of TMPc molecules involved a CASCI and RASCI-based approach, depending on the need to include ligand orbitals in the active space. In the case of CoPc, employing a minimal active space comprising solely 2p and 3d orbitals proved adequate, resulting in significant concurrence, particularly when applying a quasi-degenerate formulation of second-order corrections. Nevertheless, the situation changed for MnPc and FePc, where all computed spectra notably exhibited deficiencies, particularly evident in in-plane transitions. To explore the influence of the active space configuration, the RASCI method was utilized, yielding the introduction of novel peaks in the simulated spectra, although the agreement was found to be still poor.

Despite extensive efforts to reproduce the L-edge spectra of FePc and MnPc, it remains unclear whether the observed discrepancies arise from employing rather minimal active spaces for the acceptor orbitals considering the extensive π-conjugation and the multitude of low-lying unoccupied ligand orbitals, or from the inability to model interface and bulk properties at an isolated substrate. Current findings, along with the previous works, suggest a conclusion that involves both reasons. To elucidate the influence of the surface on the computed spectra, theoretical studies of TMPcs on surface models as well as L-edge simulations with large active spaces are currently conducted in our lab and will be reported in due course.

5. Experimental spectra

● The K-edge experimental data for 2.2 nm thick CoPc layer on graphene/Pt(111) were taken from a study by Uihlein et al., with the title "Influence of Graphene on Charge Transfer between CoPc and Metals: The Role of Graphene-Substrate Coupling".[104] This article is an open access article distributed under the terms and conditions of the Creative Commons Attribution (CC BY) license (https://creativecommons.org/licenses/by/4.0/) Copyright © 2011, American Chemical Society.

● The K-edge experimental curves of FePc on rutile TiO$_2$(110) were adapted from a previous study of Karstens et al. with the title "FePc and FePcF16 on rutile TiO$_2$(110) and (100): influence of the Substrate Preparation on the Interaction Strength".[103] Licensee MDPI, Basel, Switzerland. This article is an open access article distributed under the terms and conditions of the Creative Commons Attribution (CC BY) license (https://creativecommons.org/licenses/by/4.0/). Copyright © 2019 by the authors.

● The K-edge experimental spectra of a 3.3 nm thick MnPc layer on Ag(111) were taken from a previous study Petraki et al. with the title "Impact of the 3d Electronic States of Cobalt and Manganese Phthalocyanines on the Electronic Structure at the Interface to Ag(111)".[101] This article is an open access article distributed under the terms and conditions of the Creative Commons Attribution (CC BY) license (https://creative commons.org/licenses/by/4.0/) Copyright © 2011, American Chemical Society.

● The fluorine K-edge experimental spectra of CoPcF16 were adapted from a previous study by Petraki et al. with the title "CoPc and CoPcF16 on gold: site-specific charge-transfer processes".[97] This is an Open Access article under the terms of the Creative Commons Attribution License (https://creativecommons.org/licenses/by/2.0), which permits unrestricted use, distribution, and reproduction in any medium, provided the original work is properly cited. The license is subject to the Beilstein Journal of Nanotechnology terms and conditions: (https://www.beilstein-journals.org/bjnano).

● The fluorine K-edge experimental spectra of FePcF16 were adapted from a previous study by Belser et al. with the title "Interaction Channels Between Perfluorinated Iron Phthalocyanine and Cu(111)"[94] Copyright © 2018 Wiley-VCH Verlag GmbH & Co. KGaA, Weinheim.

● The L-edge experimental data for CoPc was taken from a previous article with the title "Communication: influence of graphene interlayers on the interaction between cobalt phthalocyanine and Ni(111)" by Uihlein et al.[100] This is an Open Access article under the terms of the Creative Commons Attribution License (https://creativecommons.org/licenses/by/2.0), which permits unrestricted use, distribution, and reproduction in any medium, provided the original work is properly cited. The license is subject to the Beilstein Journal of Nanotechnology terms and conditions: (https://www.beilstein-journals.org/bjnano).

● The L-edge experimental results for FePc were adapted from a previous study on Ag(111) surfaces with the title "Charge transfer between transition metal phthalocyanines and metal substrates: the role of the transition metal" with permission from Elsevier.[72] Copyright © 2015 Elsevier B.V. All rights reserved.

● The L-edge experimental data for MnPc was taken from a previous article with the title "Impact of the 3d Electronic States of Cobalt and Manganese Phthalocyanines on the Electronic Structure at the Interface to Ag(111)" by Petraki et al.[101] This article is an open access article distributed under the terms and conditions of the Creative Commons Attribution

20384 | Phys. Chem. Chem. Phys., 2024, 26, 20376–20387

This journal is © the Owner Societies 2024

Author contributions

Data availability

The data supporting this article have been included as part of the ESI.†

Conflicts of interest

There are no conflicts to declare.

Acknowledgements

Notes and references

1 J. Xia, R. Cao and Q. Wu, *RSC Adv.*, 2022, 1543–1550.
2 Z. Zhang, S. Yang, M. Dou, H. Liu, L. Gu and F. Wang, *RSC Adv.*, 2016, 10808–10817.
3 M. O. Senge, N. N. Sergeeva and K. J. Hale, *Chem. Soc. Rev.*, 2021, 1–32.
4 N. Lv, Q. Li, H. Zhu, S. Mu, X. Luo, X. Ren, X. Liu, S. Li, C. Cheng and T. Ma, *Adv. Sci.*, 2023, **10**, 2206239.
5 L. Milgrom, *The Colours of Life: An Introduction to the Chemistry of Porphyrins and Related Compounds*, Oxford University Press, 1997.
6 M. Wang and K. Ishii, *Coord. Chem. Rev.*, 2022, **468**, 214626.
7 M. V. Martínez-Díaz, G. de la Torre and T. Torres, *Chem. Commun.*, 2010, **46**, 7090–7108.
8 S. Reineke, M. Thomschke, B. Lüssem and K. Leo, *Rev. Mod. Phys.*, 2013, **85**, 1245–1293.
9 D. Gounden, N. Nombona and W. E. van Zyl, *Coord. Chem. Rev.*, 2020, **420**, 213359.
10 Y. Wang, X. Li and J. Yang, *Phys. Chem. Chem. Phys.*, 2019, **21**, 5424–5434.
11 J. Jiang and Ö. Bekaroğlu, *Functional Phthalocyanine Molecular Materials*, Springer, 2010.
12 S. Sanvito, *Chem. Soc. Rev.*, 2011, **40**, 3336–3355.
13 O. I. Arillo-Flores, M. M. Fadlallah, C. Schuster, U. Eckern and A. H. Romero, *Phys. Rev. B: Condens. Matter Mater. Phys.*, 2013, **87**, 165115.
14 H. Jiang, J. Ye, P. Hu, F. Wei, K. Du, N. Wang, T. Ba, S. Feng and C. Kloc, *Sci. Rep.*, 2014, **4**, 7573.
15 R. R. Cranston and B. H. Lessard, *RSC Adv.*, 2021, **11**, 21716–21737.
16 M.-S. Liao, J. D. Watts, M.-J. Huang, S. M. Gorun, T. Kar and S. Scheiner, *J. Chem. Theory Comput.*, 2005, **1**, 1201–1210.
17 P. F. Siles, T. Hahn, G. Salvan, M. Knupfer, F. Zhu, D. R. T. Zahn and O. G. Schmidt, *Nanoscale*, 2016, **8**, 8607–8617.
18 M. Urbani, M.-E. Ragoussi, M. Nazeeruddin and T. Torres, *Coord. Chem. Rev.*, 2019, **381**, 1–64.
19 I. Bruder, J. Schöneboom, R. Dinnebier, A. Ojala, S. Schäfer, R. Sens, P. Erk and J. Weis, *Org. Electron.*, 2010, **11**, 377–387.
20 M.-S. Liao and S. Scheiner, *J. Chem. Phys.*, 2001, **114**, 9780–9791.
21 L. T. Ueno, C. C. Jayme, L. R. Silva, E. B. Pereira, S. M. de Oliveira and A. E. H. Machado, *J. Braz. Chem. Soc.*, 2012, **23**, 2237–2247.
22 G. A. Peralta, M. Seth and T. Ziegler, *Inorg. Chem.*, 2007, **46**, 9111–9125.
23 K. A. Nguyen and R. Pachter, *J. Chem. Phys.*, 2001, **114**, 10757–10767.
24 J. Mack and M. J. Stillman, *J. Phys. Chem.*, 1995, **99**, 7935–7945.
25 S. Krasnikov, A. Preobrajenski, N. Sergeeva, M. Brzhezinskaya, M. Nesterov, A. Cafolla, M. Senge and A. Vinogradov, *Chem. Phys.*, 2007, **332**, 318–324.
26 X. Wang, Y. Fu, D. Tranca, K. Jiang, J. Zhu, J. Zhang, S. Han, C. Ke, C. Lu and X. Zhuang, *ACS Appl. Energy Mater.*, 2021, **4**, 2891–2898.
27 J. E. Downes, C. McGuinness, P.-A. Glans, T. Learmonth, D. Fu, P. Sheridan and K. E. Smith, *Chem. Phys. Lett.*, 2004, **390**, 203–207.
28 F. Evangelista, A. Ruocco, R. Gotter, A. Cossaro, L. Floreano, A. Morgante, F. Crispoldi, M. G. Betti and C. Mariani, *J. Chem. Phys.*, 2009, **131**, 174710.
29 T. Schwieger, H. Peisert, M. S. Golden, M. Knupfer and J. Fink, *Phys. Rev. B: Condens. Matter Mater. Phys.*, 2002, **66**, 155207.
30 N. Marom, X. Ren, J. E. Moussa, J. R. Chelikowsky and L. Kronik, *Phys. Rev. B: Condens. Matter Mater. Phys.*, 2011, **84**, 195143.
31 M. V. Nardi, F. Detto, L. Aversa, R. Verucchi, G. Salviati, S. Iannotta and M. Casarin, *Phys. Chem. Chem. Phys.*, 2013, **15**, 12864–12881.
32 I. Bidermane, I. Brumboiu, R. Totani, C. Grazioli, M. Shariati-Nilsson, H. Herper, O. Eriksson, B. Sanyal, B. Ressel, M. de Simone, L. Lozzi, B. Brena and C. Puglia, *J. Electron Spectrosc. Relat. Phenom.*, 2015, **205**, 92–97.
33 T. Kataoka, Y. Sakamoto, Y. Yamazaki, V. Singh, A. Fujimori, Y. Takeda, T. Ohkochi, S.-I. Fujimori, T. Okane, Y. Saitoh, H. Yamagami and A. Tanaka, *Solid State Commun.*, 2012, **152**, 806–809.
34 R. Kraus, M. Grobosch and M. Knupfer, *Chem. Phys. Lett.*, 2009, **469**, 121–124.
35 T. Kroll, R. Kraus, R. Schönfelder, V. Aristov, O. Molodtsova, P. Hoffmann and M. Knupfer, *J. Chem. Phys.*, 2012, **137**, 054306.

This journal is © the Owner Societies 2024

Phys. Chem. Chem. Phys., 2024, **26**, 20376–20387 | **20385**

36 T. Kroll, V. Y. Aristov, O. V. Molodtsova, Y. A. Ossipyan, D. V. Vyalikh, B. Büchner and M. Knupfer, *J. Phys. Chem. A*, 2009, **113**, 8917–8922.

37 T. Ichibha, Z. Hou, K. Hongo and R. Maezono, *Sci. Rep.*, 2017, **7**, 2011.

38 A. J. Wallace, B. E. Williamson and D. L. Crittenden, *Can. J. Chem.*, 2016, **94**, 1163–1168.

39 D. Nachtigallova, A. Antalik, R. Lo, R. Sedlak, D. Manna, J. Tucek, J. Ugolotti, L. Veis, O. Legeza, J. Pittner, R. Zboril and P. Hobza, *Chem. – Eur. J.*, 2018, **24**, 13413–13417.

40 C. Angeli, R. Cimiraglia, S. Evangelisti, T. Leininger and J.-P. Malrieu, *J. Chem. Phys.*, 2001, **114**, 10252–10264.

41 C. Angeli, R. Cimiraglia and J.-P. Malrieu, *J. Chem. Phys.*, 2002, **117**, 9138–9153.

42 C. Angeli, S. Borini, M. Cestari and R. Cimiraglia, *J. Chem. Phys.*, 2004, **121**, 4043–4049.

43 F. Neese, *Wiley Interdiscip. Rev.: Comput. Mol. Sci.*, 2018, **8**, e1327.

44 A. D. Becke, *Phys. Rev. A: At., Mol., Opt. Phys.*, 1988, **38**, 3098–3100.

45 A. D. Becke, *J. Chem. Phys.*, 1993, **98**, 5648–5652.

46 F. Weigend and R. Ahlrichs, *Phys. Chem. Chem. Phys.*, 2005, **7**, 3297–3305.

47 B. I. Dunlap, J. W. D. Connolly and J. R. Sabin, *J. Chem. Phys.*, 1979, **71**, 3396–3402.

48 O. Vahtras, J. Almlöf and M. W. Feyereisen, *Chem. Phys. Lett.*, 1993, **213**, 514–518.

49 F. Neese, *J. Comput. Chem.*, 2003, **24**, 1740–1747.

50 F. Neese, F. Wennmohs, A. Hansen and U. Becker, *Chem. Phys.*, 2009, **356**, 98–109.

51 R. Izsák and F. Neese, *J. Chem. Phys.*, 2011, **135**, 144105.

52 R. Izsák, F. Neese and W. Klopper, *J. Chem. Phys.*, 2013, **139**, 094111.

53 S. Grimme, J. Antony, S. Ehrlich and H. Krieg, *J. Chem. Phys.*, 2010, **132**, 154104.

54 S. Grimme, S. Ehrlich and L. Goerigk, *J. Comput. Chem.*, 2011, **32**, 1456–1465.

55 S. DeBeer George, T. Petrenko and F. Neese, *J. Phys. Chem. A*, 2008, **112**, 12936–12943.

56 J. Pipek and P. G. Mezey, *J. Chem. Phys.*, 1989, **90**, 4916–4926.

57 S. Hirata and M. Head-Gordon, *Chem. Phys. Lett.*, 1999, **314**, 291–299.

58 K. G. Dyall, *J. Chem. Phys.*, 1994, **100**, 2118–2127.

59 E. v Lenthe, E. J. Baerends and J. G. Snijders, *J. Chem. Phys.*, 1993, **99**, 4597–4610.

60 E. van Lenthe, E. J. Baerends and J. G. Snijders, *J. Chem. Phys.*, 1994, **101**, 9783–9792.

61 A. Chantzis, J. K. Kowalska, D. Maganas, S. DeBeer and F. Neese, *J. Chem. Theory Comput.*, 2018, **14**, 3686–3702.

62 M. Roemelt, D. Manganas, S. DeBeer and F. Neese, *J. Chem. Phys.*, 2013, **138**, 204101.

63 M. Douglas and N. M. Kroll, *Ann. Phys.*, 1974, **82**, 89–155.

64 B. A. Hess, *Phys. Rev. A: At., Mol., Opt. Phys.*, 1986, **33**, 3742–3748.

65 L. Visscher and K. G. Dyall, *At. Data Nucl. Data Tables*, 1997, **67**, 207–224.

66 W. A. de Jong, R. J. Harrison and D. A. Dixon, *J. Chem. Phys.*, 2001, **114**, 48–53.

67 N. B. Balabanov and K. A. Peterson, *J. Chem. Phys.*, 2005, **123**, 064107.

68 N. B. Balabanov and K. A. Peterson, *J. Chem. Phys.*, 2006, **125**, 074110.

69 G. L. Stoychev, A. A. Auer and F. Neese, *J. Chem. Theory Comput.*, 2017, **13**, 554–562.

70 A. Khedkar and M. Roemelt, *J. Chem. Theory Comput.*, 2019, **15**, 3522–3536.

71 A. Khedkar and M. Roemelt, *J. Chem. Theory Comput.*, 2020, **16**, 4993–5005.

72 H. Peisert, J. Uihlein, F. Petraki and T. Chassé, *J. Electron Spectrosc. Relat. Phenom.*, 2015, **204**, 49–60.

73 R. De Francesco, M. Stener and G. Fronzoni, *J. Phys. Chem. A*, 2012, **116**, 2885–2894.

74 M. K. Engel, *ChemInform*, 2003, **34**, 1–3.

75 J. Zhou, L. Zhang, Z. Hu, C. Kuo, H. Liu, X. Lin, Y. Wang, T.-W. Pi, J. Wang and S. Zhang, *AIP Adv.*, 2016, **6**, 035306.

76 J. Laurent, J. Bozek, M. Briant, P. Çarçabal, D. Cubaynes, A. Milosavljević, R. Püttner, N. Shafizadeh, M. Simon, B. Soep and G. Goldsztejn, *Phys. Chem. Chem. Phys.*, 2022, **24**, 2656–2663.

77 J. Fernández-Rodríguez, B. Toby and M. van Veenendaal, *Phys. Rev. B: Condens. Matter Mater. Phys.*, 2015, **91**, 214427.

78 K. Liu, Y. Lei and G. Wang, *J. Chem. Phys.*, 2013, **139**, 204306.

79 P. S. Miedema, M. M. van Schooneveld, R. Bogerd, T. C. R. Rocha, M. Hävecker, A. Knop-Gericke and F. M. F. de Groot, *J. Phys. Chem. C*, 2011, **115**, 25422–25428.

80 M. Linares, S. Stafström, Z. Rinkevicius, H. Ågren and P. Norman, *J. Phys. Chem. B*, 2011, **115**, 5096–5102.

81 E. B. Boydas, B. Winter, D. Batchelor and M. Roemelt, *Int. J. Quantum Chem.*, 2021, **121**, e26515.

82 T. Zhang, I. E. Brumboiu, V. Lanzilotto, J. Lüder, C. Grazioli, E. Giangrisostomi, R. Ovsyannikov, Y. Sassa, I. Bidermane, M. Stupar, M. de Simone, M. Coreno, B. Ressel, M. Pedio, P. Rudolf, B. Brena and C. Puglia, *J. Phys. Chem. C*, 2017, **121**, 26372–26378.

83 B. Brena, B. Sanyal and H. C. Herper, *J. Phys. Chem. C*, 2020, **124**, 27185–27193.

84 C. G. Barraclough, R. L. Martin, S. Mitra and R. C. Sherwood, *J. Chem. Phys.*, 1970, **53**, 1638–1642.

85 H. Yamada, T. Shimada and A. Koma, *J. Chem. Phys.*, 1998, **108**, 10256–10261.

86 S. Carlotto, M. Sambi, F. Sedona, A. Vittadini and M. Casarin, *Nanomaterials*, 2020, **11**, 54.

87 F. Petraki, H. Peisert, P. Hoffmann, J. Uihlein, M. Knupfer and T. Chassé, *J. Phys. Chem. C*, 2012, **116**, 5121–5127.

88 S. Mitra, A. K. Gregson, W. E. Hatfield and R. R. Weller, *Inorg. Chem.*, 1983, **22**, 1729–1732.

89 F. Frati, F. de Groot, J. Cerezo, F. Santoro, L. Cheng, R. Faber and S. Coriani, *J. Chem. Phys.*, 2019, **151**, 064107.

20386 | *Phys. Chem. Chem. Phys.*, 2024, **26**, 20376–20387

This journal is © the Owner Societies 2024

90 A. Banerjee, V. V. da Cruz, V. Ekholm, C. Såthe, J.-E. Rubensson, N. Ignatova, F. Gel'mukhanov and M. Odelius, *Phys. Rev. A*, 2023, **108**, 023103.

91 J. Stierhof, S. Kühn, M. Winter, P. Micke, R. Steinbrügge, C. Shah, N. Hell, M. Bissinger, M. Hirsch, R. Ballhausen, M. Lang, C. Gräfe, S. Wipf, R. Cumbee, G. L. Betancourt-Martinez, S. Park, J. Niskanen, M. Chung, F. S. Porter, T. Stöhlker, T. Pfeifer, G. V. Brown, S. Bernitt, P. Hansmann, J. Wilms, J. R. Crespo López-Urrutia and M. A. Leutenegger, *Eur. Phys. J. D*, 2022, **76**, 38.

92 G. Mangione, S. Carlotto, M. Sambi, G. Ligorio, M. Timpel, A. Vittadini, M. V. Nardi and M. Casarin, *Phys. Chem. Chem. Phys.*, 2016, **18**, 18727–18738.

93 G. Mangione, M. Sambi, S. Carlotto, A. Vittadini, G. Ligorio, M. Timpel, L. Pasquali, A. Giglia, M. V. Nardi and M. Casarin, *Phys. Chem. Chem. Phys.*, 2016, **18**, 24890–24904.

94 A. Belser, R. Karstens, P. Nagel, M. Merz, S. Schuppler, T. Chassé and H. Peisert, *Phys. Status Solidi B*, 2019, **256**, 1800292.

95 M. Klues, P. Jerabek, T. Breuer, M. Oehzelt, K. Hermann, R. Berger and G. Witte, *J. Phys. Chem. C*, 2016, **120**, 12693–12705.

96 D. G. de Oteyza, A. Sakko, A. El-Sayed, E. Goiri, L. Floreano, A. Cossaro, J. M. Garcia-Lastra, A. Rubio and J. E. Ortega, *Phys. Rev. B: Condens. Matter Mater. Phys.*, 2012, **86**, 075469.

97 F. Petraki, H. Peisert, J. Uihlein, U. Aygül and T. Chassé, *Beilstein J. Nanotechnol.*, 2014, **5**, 524–531.

98 P. S. Miedema, S. Stepanow, P. Gambardella and F. M. F. de Groot, *J. Phys.: Conf. Ser.*, 2009, **190**, 012143.

99 J. Lüder, *Phys. Rev. B*, 2021, **103**, 045140.

100 J. Uihlein, H. Peisert, M. Glaser, M. Polek, H. Adler, F. Petraki, R. Ovsyannikov, M. Bauer and T. Chassé, *J. Chem. Phys.*, 2013, **138**, 081101.

101 F. Petraki, H. Peisert, F. Latteyer, U. Aygül, A. Vollmer and T. Chassé, *J. Phys. Chem. C*, 2011, **115**, 21334–21340.

102 D. Balle, H. Adler, P. Grüninger, R. Karstens, R. Ovsyannikov, E. Giangrisostomi, T. Chassé and H. Peisert, *J. Phys. Chem. C*, 2017, **121**, 18564–18574.

103 R. Karstens, M. Glaser, A. Belser, D. Balle, M. Polek, R. Ovsyannikov, E. Giangrisostomi, T. Chassé and H. Peisert, *Molecules*, 2019, **24**, 4579.

104 J. Uihlein, M. Polek, M. Glaser, H. Adler, R. Ovsyannikov, M. Bauer, M. Ivanovic, A. B. Preobrajenski, A. V. Generalov, T. Chassé and H. Peisert, *J. Phys. Chem. C*, 2015, **119**, 15240–15247.

This journal is © the Owner Societies 2024

Phys. Chem. Chem. Phys., 2024, **26**, 20376–20387 | **20387**